MDPI

Article

Ice-Water-Gas Interaction during Icebreaking by an Airgun Bubble

Qi-Gang Wu [1], Zuo-Cheng Wang [1], Bao-Yu Ni [1,*], Guang-Yu Yuan [1], Yuriy A. Semenov [2], Zhi-Yuan Li [3]
and Yan-Zhuo Xue [1]

1   College of Shipbuilding Engineering, Harbin Engineering University, Harbin 150001, China
2   Institute of Hydromechanics, National Academy of Sciences of Ukraine, 03680 Kyiv, Ukraine
3   Department of Mechanics and Maritime Sciences, Chalmers University of Technology,
    SE-41296 Gothenburg, Sweden
*   Correspondence: nibaoyu@hrbeu.edu.cn

Abstract: When an airgun releases high-pressure gas underwater below an ice plate, it is observed that a bubble is formed rapidly while the ice plate is broken fiercely. In order to study the ice-water-gas interaction during this transient and violent phenomenon, a set of laboratory-scale devices was designed and a series of icebreaking experiments were carried out. High-speed photography was used to capture the evolution of the bubble and the ice plate. It was found that the airgun bubble had a unique 'pear' shape compared with the spherical bubble generated by electric sparking. The pressure induced by the pulsation of the airgun bubble near a rigid wall was measured by the pressure sensor. The initial shockwave, oscillatory pressure peaks caused by the directional fast air injection, secondary shockwave, and pressure peak caused by the bubble jet impact were clearly recorded. Three damage patterns of ice plates were observed and corresponding reasons were analyzed. The influence of dimensionless parameters, such as airgun-ice distance H and ice thickness T, was also investigated. The physical mechanism of ice-water-gas interaction was summarized.

Keywords: airgun; high-pressure gas; bubble dynamics; icebreaking; experimental study

1. Introduction

Improving icebreaking efficiency is a hot topic in polar research. The traditional ice breaking method mainly relies on the hull structure to impact the ice layer [1–3], which may cause structural damage and even induce 'icebound' or 'ice collision' accidents [4,5]. By virtue of intense loading, high-pressure bubbles have been studied and adopted in auxiliary icebreaking in recent years [6–8]. Compared with the traditional method, the icebreaking by an airgun bubble can comprehensively utilize a variety of loads [9,10] and be more environmentally friendly [11], including for mammals [12]. Icebreaking making use of high-pressure bubbles involves complex ice-water-gas interaction, such as the propagation of shock waves in fluid and ice, the dynamic development of the water-gas interface, and various damaging modes of ice under combined loads, etc. It is thus considered as a challenging subject and requires in-depth studies.

There are many methods to produce underwater high-pressure bubbles, such as using an electric spark, explosion, and a high-pressure airgun. An electric spark bubble is usually used in laboratories and has become an effective method for mechanism experimentation of bubble sources [13–15]. Cui et al. [8] conducted an icebreaking experiment using spark bubbles in an open water tank and verified the feasibility of icebreaking by using underwater bubbles. This experiment carefully observed the changes in fluid pressure during the whole process of bubble development, including the first shock wave, bubble jet, secondary shock wave, etc. The generation and development of ice cracks under these loads were recorded and analyzed. Yuan et al. [10] conducted ice-breaking experiments by using spark bubbles in a cold room. Four ice-breaking modes under various parameter combinations

were found. Ni et al. [7] further used spark bubbles to break an ice floe with a hole experimentally. The effect of the initial hole on the ice floe was studied and it was found that the hole made the ice floe more likely to be broken by the initial shock wave. The breaking mechanism of an ice floe with and without an initial hole was compared. In addition to experimental study, numerical simulations on icebreaking by using spark bubbles were also developed. For example, Ni et al. [6] and Kan et al. [9] studied the interaction between a spark bubble and an ice plate by using a combination of the Boundary Element Method (BEM) and peridynamics. In their work, the BEM approach was employed to simulate bubble dynamics and loads, whereas the peridynamics approach was utilized to study the response of ice under bubble loads. The full interaction of bubble and ice was nevertheless not investigated, because only bubble loads were exerted on the ice.

Underwater explosions are usually used in field experiments to generate bubbles [16] and have been extensively adopted in river ice blasting [17]. Barash [18], from the US Naval Ordnance Laboratory (NOL), studied the influence of the weight of charge, the distance under the ice, and the thickness of the ice on the icebreaking effect through many underwater explosive icebreaking experiments. Mellor [19,20], from the US Army Cold Zone Research and Engineering Laboratory (CRREL), summarized past experimental data and analyzed the relationship between the icebreaking radius and the explosive weight, the distance under the ice, and the thickness of the ice floes. After dimensionless and regression analysis of the data, the empirical formula of the icebreaking radius was developed. Wang et al. [21] utilized the Arbitrary-Lagrangian-Eulerian (ALE) technique to solve the Fluid-Structure Interaction (FSI) processes between the fluid and ice structures during ice-breaking by using underwater explosion bubbles. They calculated the correlation coefficient and correlation degree between the icebreaking radius and three factors, namely charge, blast distance, and ice thickness. The accuracy of the numerical method was verified by comparing it with experimental results. Wang et al. [22] further compared the ice damage characteristics under single explosive and multiple explosives by numerical study, finding that the ice-breaking efficiency of the two explosives with a suitable spacing distance in the horizontal direction is higher than that of a single explosive with an equal charge.

In comparison with bubbles generated from electric sparking and underwater explosion, high-pressure airgun bubbles are less studied and have mainly been used in seabed resource exploration [23]. Giles [24] used a device comprised of eight to twenty-three airguns, which released airgun bubbles to obtain the sample sections of marine seismic exploration in the Gulf of Mexico and the Pacific Ocean offshore California. Chen et al. [25] used high-pressure airgun bubbles to generate seismic waves to detect seabed structures and conditions. To meet the environmental requirement for a deep-water seismic survey, Chelminski et al. [26] designed new airguns that can increase the low-frequency component of the signal. In the icebreaking field by using high-pressure air bubbles, only a few very early research literatures are available. Mellor and Kovacs [27] conducted experimental studies of gas blasting devices to break the floe ice. The composition of the high-pressure gas was carbon dioxide. The results were compared with conventional chemical explosives. The study found that the floe ice was mainly damaged in bending strength and the diameter of the broken ice was larger than that of conventional chemical explosives. Joseph et al. [28] systematically introduced an underwater high-pressure gas ice-breaking device based on a mixture of air and fuel (propane). The device was installed at the bow of a barge and an actual ice-breaking effect under different influencing factors was observed. This type of experimental research mainly focused on icebreaking by shock wave but did not pay attention to other typical loads such as bubble jets, pulsations, and so on.

In this work, the authors conducted an experimental study on ice-water-gas interaction during the icebreaking process using bubbles, with the aim of a better understanding of the icebreaking mechanism of airgun bubbles. For this purpose, a laboratory-scale airgun icebreaking device was developed and a series of icebreaking experiments were carried out to study ice-water-gas interaction as well as damage patterns of the ice plate under various parameters.

2. Experimental Set-Up and Principles

2.1. The Laboratory-Scale Airgun

A laboratory-scale airgun was developed. In general, it is divided into two parts, the air storage chamber, and the solenoid valve, as shown in Figure 1. The diameter and the length of the air gun was 43 mm and 225 mm, respectively, and the exhaust port was in the middle of the air gun body. The capacity of the air storage chamber was 50 mL, approximately, and the working pressure was 0~10 MPa, which can be adjusted within the design allowance. The airgun worked by releasing a certain amount of compressed gas into the water through the exhaust port in an instant, under the action of mechanical movement controlled by the solenoid valve. The detailed mechanical movement of all the elements of the airgun system in Figure 1 can refer to the patent [29]. Different from the traditional airgun with multi exhaust ports [30], only one single exhaust port was designed in the middle of the airgun. In this way, a single bubble with a clear gas-water interface can be obtained and the coalescence of multi bubbles generated from multi ports in the traditional airgun can be avoided. For the gas flow speed, one can estimate it [31] by using the empirical formula as below

$$\frac{dm}{dt} = \tau \sqrt{\frac{m_g(P_0 - P_b)}{V_0}} \tag{1}$$

where P_0 is the working pressure of the airgun, V_0 is the volume of the airgun, m_g is the amount of gas, P_b is the pressure inside the bubble and τ is a coefficient based on the airgun design. However, it is hard to determine the coefficient τ by using experimental data directly, because it is hard to observe when the gas has been released completely from gas chamber into water or bubble. This parameter will be studied specially in future work.


(a)
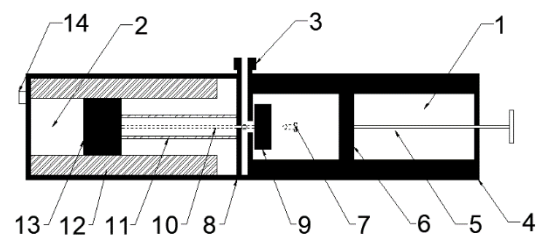
(b)

Figure 1. Equipment of the airgun: (1) air storage chamber, (2) solenoid valve, (3) exhaust port, (4) cylinder body, (5) capacity control rod, (6) piston seal, (7) intake port, (8) solenoid valve outer shell, (9) sealing element, (10) movable bar, (11) reset spring, (12) electromagnetic coil, (13) cast iron, (14) wire interface. (**a**) real objects, (**b**) schematic view.

2.2. Experimental Set-Up

Figure 2 provides the photo and schematic view of the whole experimental set-up. According to functions, the experimental set-up can be divided into three parts: airgun system, observation system, and structural system. As shown in Figure 2b, the airgun system was mainly composed of the airgun (see Figure 1), compressor, air tank, gas piping, and control system. Among them, the air tank consisted of a set of ten pressure vessels, which can provide a total air capacity of 20 L approximately and sustain the stability of the pressure of compressed air.
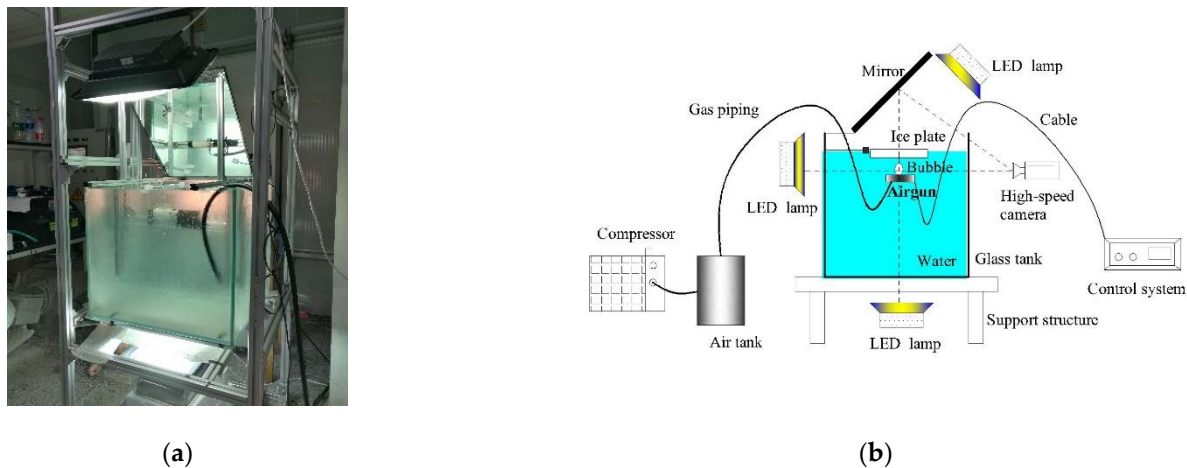
Figure 2. Experimental set-up. (**a**) real objects, (**b**) schematic view.

The observation system included a high-speed camera, a mirror, and three LED lamps. A Photron Mini AX100 high-speed camera was used to record the whole process, which can provide 4000 frames per second (fps) at a High-definition (HD) resolution of 1280×1024 pixels, or a maximum photographic speed of 204,800 fps. During the process of the experiment, we needed to record the change of the bubble behavior from the side view and the development of ice crack from the top view simultaneously. In order to achieve this aim with one high-speed camera, a plane mirror was used to shoot the side view and the top view at the same time [32], as shown in Figure 2. Three LED lamps were used to provide enough light in the experiment.

The structural system included a water tank and support framework, as shown in Figure 2a. The square water tank was made of glass of 12 mm and the principal dimensions were $600 \times 600 \times 600$ mm^3. The distances between the bubble surface and the tank walls were large enough compared with the bubble diameter, so the boundary effect of the tank wall can be ignored. The water depth was 580 mm and the distance of the exhaust port of the airgun below the free surface could be adjusted according to working conditions. An air-free ice plate was prepared by degassed water and located on the free surface of the water. Then, the experiment could start and the dynamic change of ice-water-gas interaction was recorded and analyzed. The ice sample used in this paper was a circular ice plate with a diameter of 380 mm, and the thickness depended on the requirements of the test. The detailed preparation process, as well as the mechanical properties of the ice plate, can refer to Yuan et al. [10] and Ni et al. [29]. The bending strength was 2.39 MPa by the three-point bending test. The Young's modulus was 6.25 GPa and compressive strength was 9.41 MPa by the uniaxial compression test. Other physical properties are suggested to refer to those of freshwater at the same temperature (-5 °C) for reference. For example, Poisson's ratio can be taken as 0.33 from recommendation of Hobbs [33]. The water temperature during the test was about 10 °C and the pressure of the surrounding liquid was hydrostatic pressure, which was about 1.96 kPa for the exhaust port with a submergence depth of 0.2 m.

2.3. Bubble Shape and Nondimensionalization

As the high-pressure gas was released from the unilateral exhaust port of the airgun, the gas velocity was not uniform around but had a strong directivity. As a result, unlike the spark or explosion bubble with a spherical shape in the expansion stage, the airgun bubble was not spherical but in a 'pear-like' shape in the expansion stage, as shown in Figure 3. The largest horizontal diameter d_{max} (corresponding to the largest volume) of this pear-shaped bubble in a free field is an important physical quantity. d_{max} was measured by using a postprocessing software of Photron camera, which can measure the distance between two points referring to a scale plate. The picture corresponding to the largest volume of the

bubble was selected, before the software was adopted to measure the horizontal distance between two outermost points (left and right) on the bubble surface, as shown in Figure 3. Each d_{max} was measured at least three times. The average value was chosen as d_{max} and the uncertainty was found no more than 2.6% d_{max} for all the cases. d_{max} was determined by the working pressure P_0 directly. As long as one knows the variation law of d_{max} and P_0, the ice-breaking capability of the airgun bubble can be quantized by using d_{max} instead of P_0.
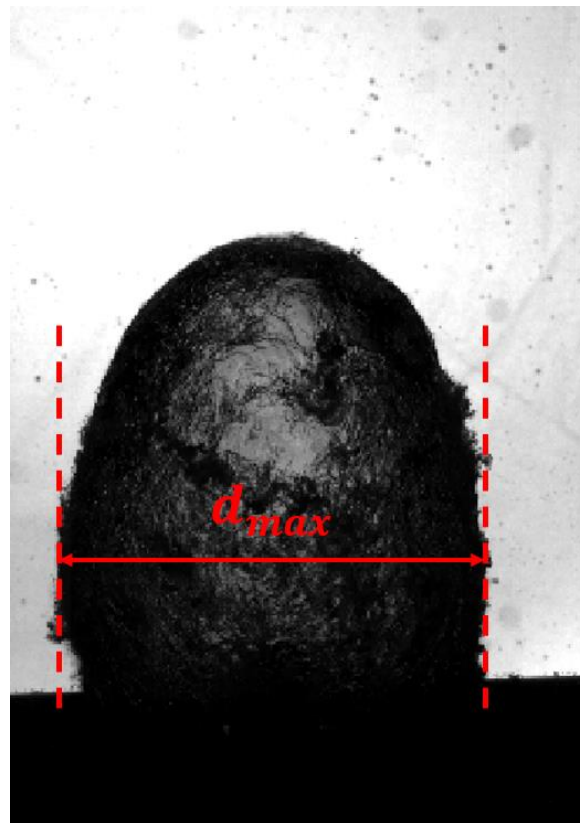
Figure 3. The 'pear-like' shape of the airgun bubble in a free field.

According to energy conservation before shot and maximum bubble volume after shot, one can derive a simplified relation between d_{max} and P_0. Just before the shot, there is potential energy, E_p, conserved in the bubble [34–36] as

$$E_p = c_1 P_0 V_0 \tag{2}$$

where V_0 is the volume of the air gun, P_0 is working pressure, and c_1 is a coefficient for the design of the gun. When the bubble achieves the maximum, the moving velocity of the bubble at that moment is zero, so the kinetic energy is zero and the potential energy [34–36] can be written as

$$E_p = c_2 P_h V_{max} = c_3 P_h d_{max}^3 \tag{3}$$

where V_{max} is the maximum volume of the bubble, P_h is the hydrostatic pressure, and c_2 and c_3 are coefficients related to bubble shape, and so on. Considering energy conservation between Equations (2) and (3), one can obtain the link between d_{max} and P_0 as

$$d_{max} = c_4 (P_0 V_0 / P_h)^{1/3} = C P_0^{1/3} \tag{4}$$

where c_4 and C are coefficients.

A series of experiments of the airgun bubble in a free field under different P_0 were done and the results were presented in Figure 4. To determine the coefficient C, we fitted

the curve in Figure 4 and found C approximate to $5.04 \times 10^{-4} \text{mPa}^{-1/3}$ here. Therefore, it is easy to understand that $d_{\max}$ rises along with P_0 and the rise of $d_{\max}$ gets slow when P_0 gets large.
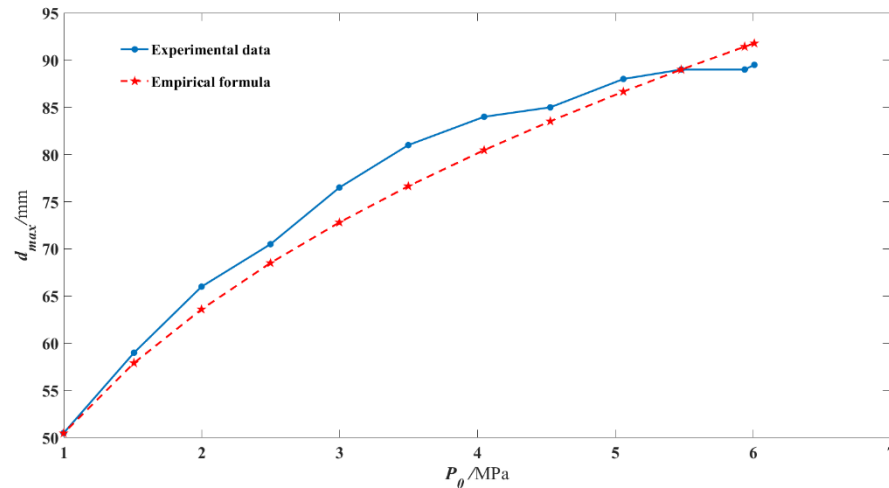

Figure 4. Variation law of $d_{\max}$ along with P_0 in a free field.

As $d_{\max}$ is an important parameter in studying bubble behaviors [37], it was chosen as the characteristic length to nondimensionalize other parameters as below:

$$H = h/d_{\max} \tag{5}$$

$$T = t/d_{\max} \tag{6}$$

where H is distance parameter and T is ice thickness parameter, h is the distance between the lower surface of the ice plate and the upper surface of the exhausting port, and t is the ice thickness, as shown in Figure 5.
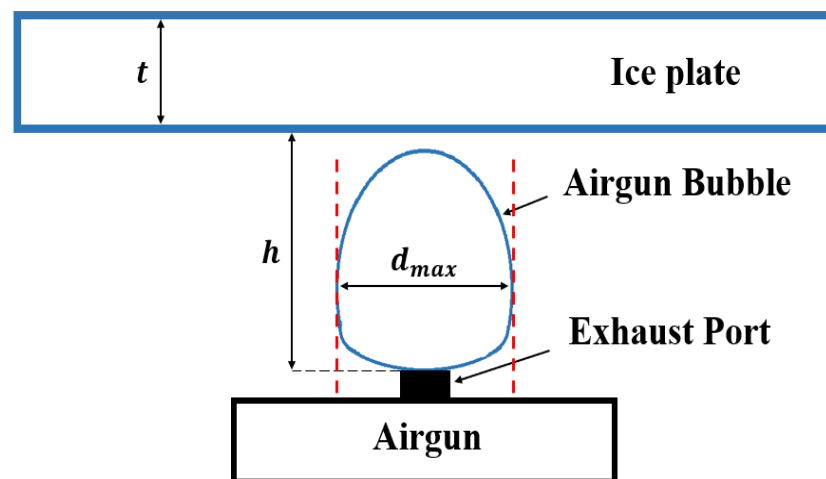
Figure 5. Schematic of dimensionless parameters.

3. Results and Discussions

3.1. Pressure Measurement

In the ice breaking experiment by using an airgun bubble, the ice plate could be regarded as a complete wall before it was broken. Therefore, it was helpful to study and analyze the pressure characteristics induced by a high-pressure airgun bubble near a rigid wall, which will provide a foundation of load characteristics for icebreaking. In this section, the rigid wall was simulated by an aluminum circular plate with a diameter of 380 mm and

a thickness of 10 mm. A wall pressure sensor was placed at the center of the aluminum plate perforated. The model of the pressure sensor was PCB 113b21. The working pressure of the airgun P_0 was 1.52 MPa and the explosion distance h was 52 mm. The shooting frequency was 20,000 frames/s, and the typical photos of the case were shown in Figure 6 at different moments. The time-history curve of measured pressure P_m in the center of the plate was presented in Figure 7, in which P_m was relative pressure with an initial value of 0 kPa.
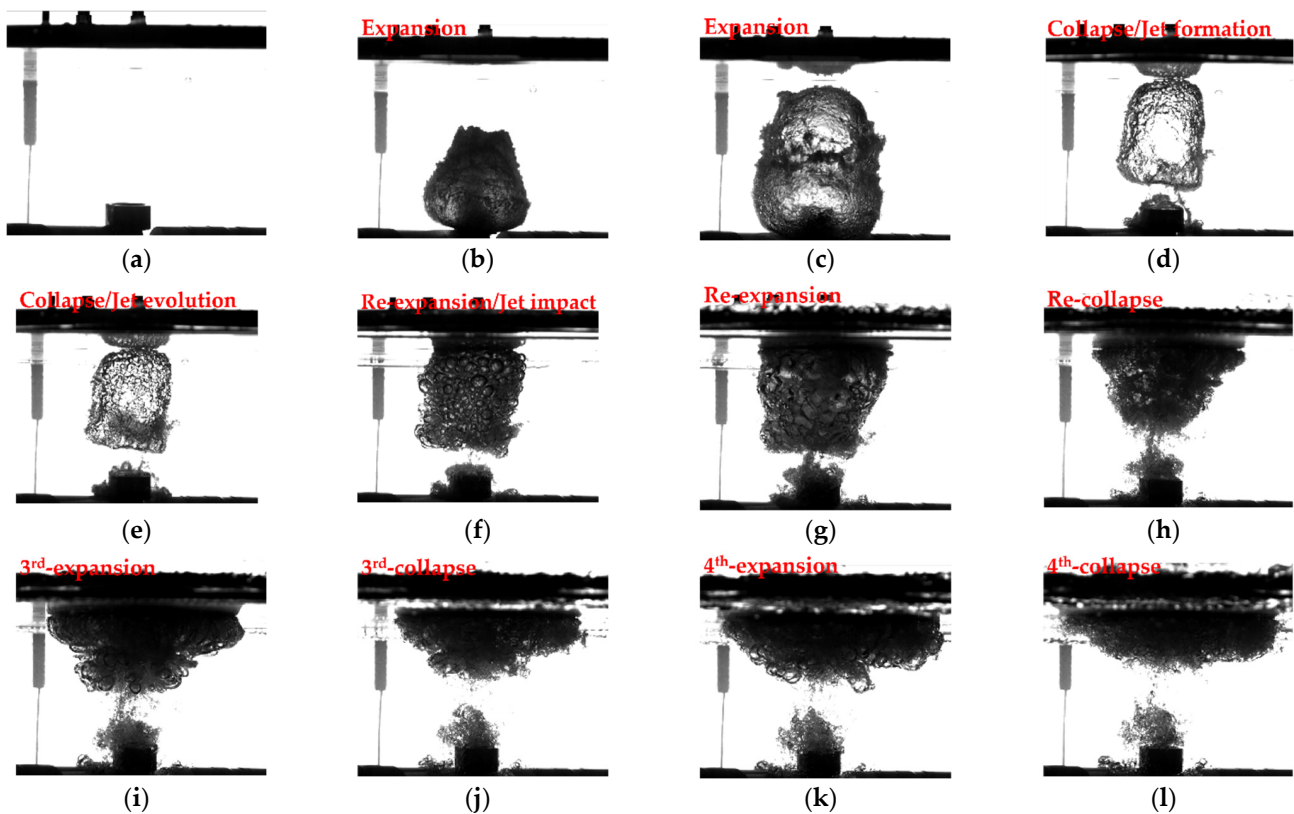
Figure 6. Image of underwater airgun bubble near a rigid wall. (**a**) $t = 0$ ms, (**b**) $t = 1.95$ ms, (**c**) $t = 5.00$ ms, (**d**) $t = 8.35$ ms, (**e**) $t = 8.85$ ms, (**f**) $t = 10.80$ ms, (**g**) $t = 13.35$ ms, (**h**) $t = 16.00$ ms, (**i**) $t = 18.90$ ms, (**j**) $t = 23.65$ ms, (**k**) $t = 27.35$ ms, (**l**) $t = 31.05$ ms.
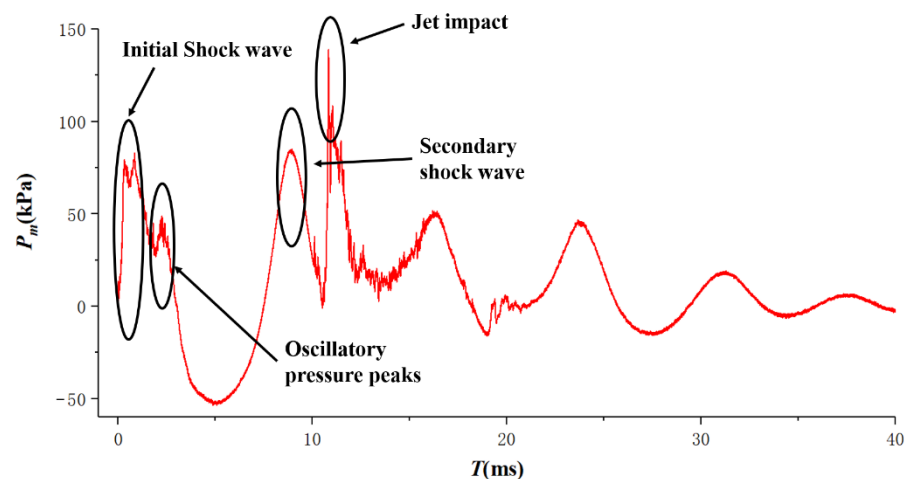
Figure 7. The pressure in the center point of the aluminum plate.

Initially, when the compressed gas was released into water, an initial shock wave was generated immediately. The directional fast air jet pushes the water impacting on the wall continuously and rapidly, forming a transient vortex in front of the wall [38,39]. Under this water impact, several oscillatory pressure peaks were observed right after the initial shockwave, whose duration was around 1–2 ms. These oscillatory pressure peaks were not observed by previous experiments of spark bubble or underwater explosion bubble [40,41], which indicated that the directional fast air jet indeed caused the change of flow field and induced strong additional pressure loads. It is expected that these oscillatory pressure peaks would aggravate the damage of ice. Then a 'pear-like' bubble was formed and the induced pressure became stable and declined smoothly until the first bottom at 5 ms, when the bubble reached a maximum volume in the first expansion as shown in Figure 6c. One may notice that there was a part of bubble structure directly attached to the plate, which was just a mirrored image of the original bubble due to the reflection of the smooth aluminum plate surface (same for the subsequent pictures). After that, the airgun bubble collapsed under pressure difference, while the induced pressure rose smoothly. In the process of bubble collapse, the lower part of the bubble started to separate from the exhaust port of the airgun and got to involute as shown in Figure 6d. The detailed development process of involute bubble surface was recorded in Appendix A along with the variation of the bubble volume. As a result, an upward jet started to be generated under the combined effects of attraction force of the wall and buoyancy force. Then the bubble reached a minimum volume around 8.85 ms as shown in Figure 6e. At this moment, the secondary shock wave [42] was released as marked in Figure 7. The upward jet moved further but did not penetrate the bubble yet. After the first minimum volume, the bubble started to re-expand and its surface started to become unsmooth distinctly. At around 10.80 ms in Figure 6f, the jet penetrated the bubble and impacted on the surface of the aluminum plate directly. The direct impact of the jet resulted in a pressure peak sharply on the wall surface [43], as marked in Figure 7. It can be seen that the pressure impulse induced by the jet impact was even higher than that induced by the shock wave, which was expected to contribute to icebreaking. Subsequently, the remaining bubble expanded and collapsed repeatedly and the surface became more and more instable. At the same time, the induced pressure became weaker and weaker as shown in Figure 7. Finally, the bubble would dissipate.

3.2. Typical Case Study

In this section, a case was chosen to study the full development of ice-water-gas interaction during the ice-breaking process. The parameters adopted in this section were as follows: the thickness of the circular ice plate was 17 mm, the initial pressure of the high-pressure airgun was 1.7 MPa, the air storage chamber's volume was 50 mL, the explosion distance was 65.5 mm, and the maximum horizontal diameter of the air gun bubble d_{m} was measured as 64.2 mm. Under this working condition, the distance parameter H was 1.02 and the ice thickness parameter T was 0.28. Figure 8 provided the development of the bubble and the ice plate, in which each picture included both the top and side view. The upper part of the picture was a top view, which was mainly used to observe the crack propagation and failure patterns of the ice plate under the high-pressure airgun bubble, whereas the lower part was a side view, which was mainly used to observe the motions of the bubble and free surface. Each picture had a corresponding moment below it.

As per Figure 8a–c, the airgun released high-pressure got into water and formed a 'pear-shaped' bubble. The bubble expanded before reaching a maximum volume firstly in Figure 8c. The top of the bubble did not contact the ice plate and the ice plate was kept intact. Because the pressure of the bubble was lower than the ambient water pressure when the bubble reached maximum under inertia, the bubble would shrink under the ice surface, as shown in Figure 8c–f. Meanwhile, the bubble approached the ice surface under the action of buoyancy and attraction of the ice plate. As a result, under the action of pressure difference, the lower surface of the bubble moved faster towards the ice than the upper surface of the bubble and involuted into the bubble. The jet was generated as a result, as

marked in Figure 8e. When the high-pressure bubble collapsed to the minimum volume, the ice plate was damaged and radial cracks appeared, which could be seen in Figure 8f. Then the bubble re-expanded, as shown in Figure 8g. The bubble still moved towards the ice surface and touched the lower surface of the ice plate. Under the action of expansion of the bubble, the outward motion of the fluid expanded the cracks of the ice plate a little. After several re-expansions and re-collapses, the bubble rose to the lower surface of the ice and the jet impacted the ice directly, as shown in Figure 8h, followed by a retarded flow. One could see that the free surface rose and the ice plate started to break up under the impact of the bubble and retarded flow. Finally, the bubble burst at the free surface and a distinct free-surface 'spike' was formed as marked in Figure 8i. This free-surface 'spike' or water 'hump' was formed under the combined effects of gas releasing, a coalesce of bubbles and free surfaces, buoyancy, and inertial forces, etc. It pushed the ice fragments turning up and expanded the crevasse of the ice plate. Finally, the gas was released into the air and the bubble dissipated as shown in Figure 8j.
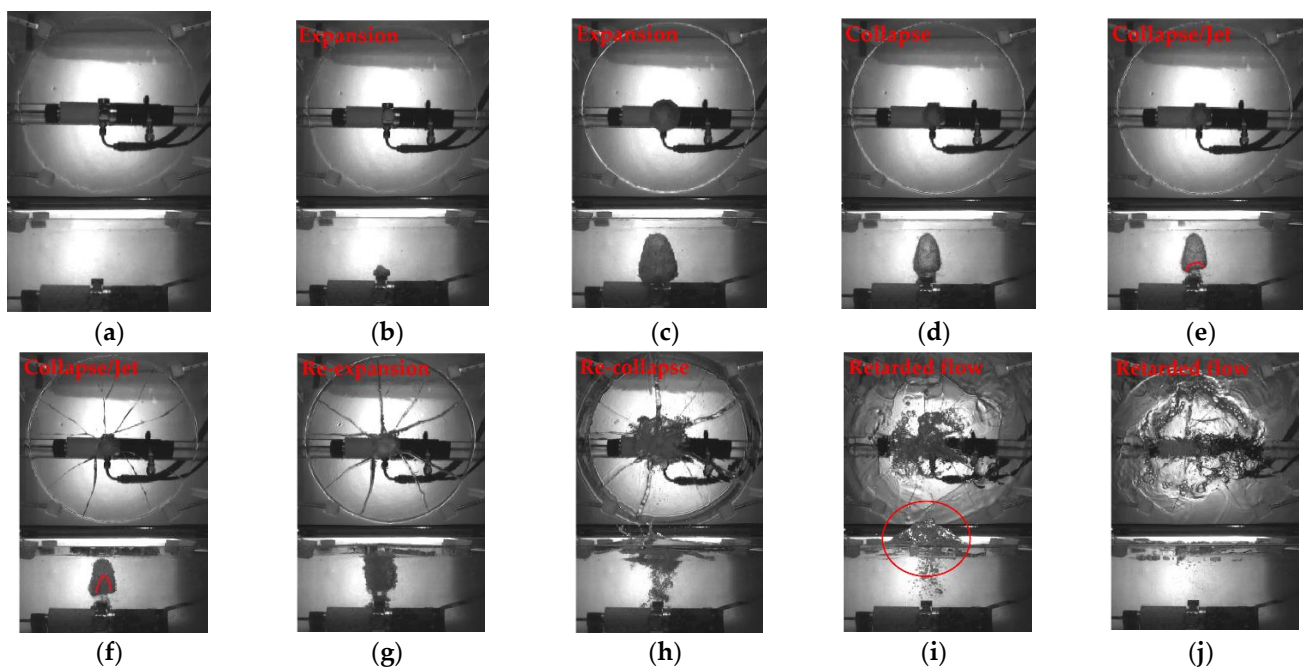
Figure 8. Images of icebreaking by an airgun bubble with $T = 0.28$ and $H = 1.02$. (**a**) $t = 0$ ms, (**b**) $t = 0.60$ ms, (**c**) $t = 4.80$ ms, (**d**) $t = 8.65$ ms, (**e**) $t = 9.20$ ms, (**f**) $t = 9.90$ ms, (**g**) $t = 16.35$ ms, (**h**) $t = 69.10$ ms, (**i**) $t = 215.05$ ms, (**j**) $t = 423.95$ ms.

The mechanical reason for the damage to the ice plate was analyzed, referring to the high-pressure bubble loads near a rigid wall in Figure 7. Initially, a shock wave was generated along with the bubble generation. Because the explosion distance was large in this case, the shock wave attenuated very soon in the propagation [44] and became too weak to break the ice when it arrived at the ice plate. The secondary shock wave was generated when the bubble reached the minimum value. On the one hand, the second shock wave, which was released from the center of the bubble, was nearer to the ice plate compared with the first shock wave. On the other hand, the bubble jet impacted the ice plate immediately following the secondary shockwave also, which can be predicted by the jet moving tendency in Figure 8e,f. As a result, the ice plate was damaged under the combined effects of the second shock wave and the bubble jet loads, showing radial cracks on it, as shown in Figure 8f. A similar phenomenon was also found in icebreaking by using a spark bubble [7,10]. Compared with a spark bubble, an airgun bubble had more cycles and generated more shock waves with damping amplitudes. Moreover, the separated cracks or slits made the free surface appear among the ice fragments. The interaction

between the free surface and airgun bubble, involving retarded flow and free-surface spike, aggravated the fracture of the ice plate.

3.3. The Damage Patterns of Ice under Airgun Bubble Loads

According to different experimental results, icebreaking was divided into several patterns, including radial slits pattern, radial and circumferential slits pattern, radial cracks pattern, and no crack pattern. The following are detailed descriptions of these results.

(1) Radial slits pattern

Based on the typical case in Section 3.2, if we further reduced the distance between the exhaust port and the ice surface, the situation as shown in Figure 9 would occur, in which the ice plate was broken up along the radial slits. The radial cracks could be either generated by the initial shock wave, or the secondary shock wave along with a bubble jet, such as the typical case in Figure 8. For the former, the initial release of high-pressure gas induced high-speed shockwave transmission during the water phase (gas-water interaction). The shockwave transmitted and reflected at the water-ice interface and induced a stress wave transmission during the ice plate, which transmitted and reflected at the ice-gas interface (water-ice-gas interaction). When the induced stress (either compressive or tensile stress) exceeded the allowable stress of the ice plate, cracks were generated. For the latter case, the induced stress in the ice plate caused by the initial shockwave was not strong enough to break ice, but that caused by a closer secondary shock wave and the pressure peak induced by the impact of bubble jet was strong enough to break ice. In either case, when radial cracks occurred, a retarded flow, formed by a large amount of gas and water, separated the cracks into slits. Once slits were generated, the free surface appeared and interacted with the bubble and ice, inducing a free-surface spike which pushed large pieces of broken ice fragmented. Therefore, this pattern was named as a 'radial slits pattern', in which the case with radial slits coming from the first shock wave was in short for the 'radial slits (shock wave)' pattern, whereas the case with radial slits coming from secondary shock wave and bubble jet was in short for the 'radial slits (jet)' pattern. In these two patterns, the potential energy of high-pressure gas transformed into the kinetic and potential energy of water and fracture energy of the ice plate as well as the kinetic energy of ice fragments mainly. All interfaces of media including bubble, free-surfaces, and ice plates evolved fiercely under complex gas-water-ice interaction.
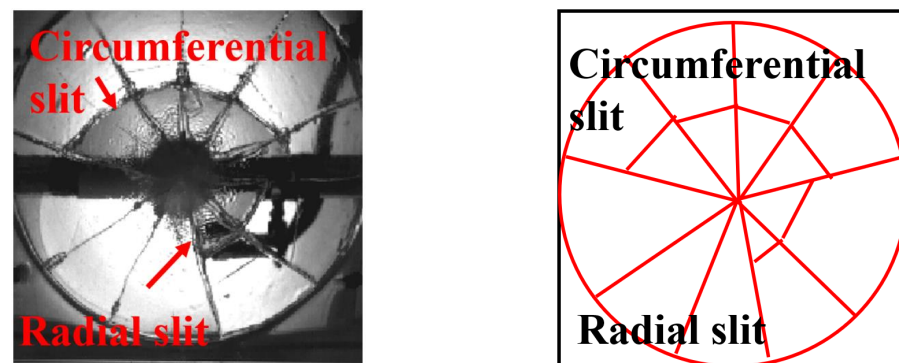

Figure 9. Radial slits pattern when $H = 0.53$, $T = 0.27$.

(2) Radial and circumferential slits pattern

Based on the 'radial slits pattern' case in Figure 9, if we further reduced the ice thickness, the pattern as shown in Figure 10 may appear, in which both radial and circumferential slits were formed. There were two situations for this pattern. For the first case, when the distance parameter was small enough ($H \leq 0.6$), the initial shock wave generated high radial and tangential stress at the same time, and induced the radial and circumferential cracks almost simultaneously. For the second case, under appropriate parameters (for example $H \approx 1.0$, $T \approx 0.18$), the initial shock wave could only cause radial cracks on the ice

plate, whereas the secondary shock wave and bubble jet would generate circumferential cracks based on radial cracks. In either case, the cracks would eventually expand into slits under the action of retarded flow. Therefore, this pattern was named as the 'radial and circumferential slits pattern'. In this pattern, the case with circumferential slits coming from the first shock wave was short for 'radial and circumferential (shock wave) slits', whereas the case with circumferential slits coming from secondary shock wave and bubble jet was short for 'radial (shock wave) and circumferential (jet) slits' patterns. For this pattern, the triangular ice fragments inside the circumferential cracks may be uplifted at the vertex of the triangle, namely the center of the ice plate, whereas the ice fragments outside the circumferential cracks were almost kept motionless. Thus, the kinetic energy of ice fragments became much smaller than other energy compared with the pattern in Figure 9.

Figure 10. Radial and circumferential slits pattern when *H* = 0.59, *T* = 0.17.

(3)   Radial cracks pattern

On the basis of the typical case in Section 3.2, if we further increased the distance between the exhaust port and the ice surface, the situation as shown in Figure 11 may occur, in which the ice plate did not break up but only had several radial cracks on it. Similar to the typical case in Figure 8, the initial shock wave could not break the ice plate because of large distance and sharp attenuation. The radial cracks were caused by the secondary shock wave and bubble jet. Different from the separated cracks or slits in Figure 8, the cracks in Figure 10 were quite slight. One could see that the collapsing bubbles were trapped under the ice plate, which indicated that the cracks did not penetrate the ice plate. This type of crack was also named 'non-through cracks' [29,45]. Actually, the ice plate still kept as a whole in this case. This pattern was named as 'radial cracks pattern'. In this pattern, fracture energy of the ice plate became much smaller than that in the pattern in Figure 10 and kinetic energy of ice fragments was little.
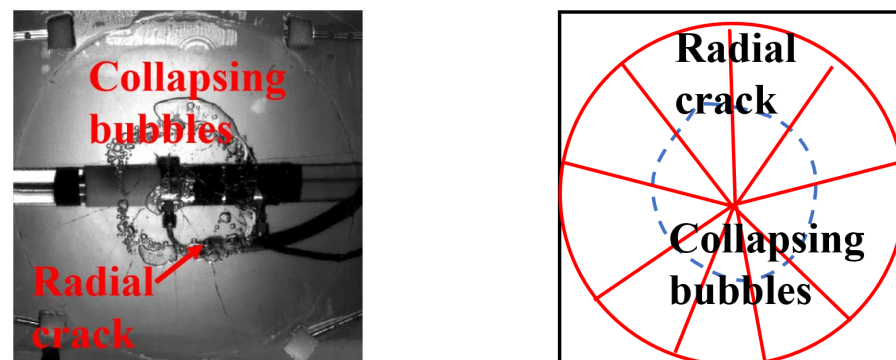
Figure 11. Radial cracks pattern when *H* = 1.49, *T* = 0.28.

(4)   No crack pattern

When the distance parameter was very large, and/or the ice thickness parameter was very large, the ice may not be broken, as shown in Figure 12. In this case, there would be

no crack and obvious change on the ice plate, or the ice plate was kept intact. Meanwhile, bubbles were trapped and attached to the lower surface of the ice plate after collapsing, as shown in Figure 12. In this pattern, there was no fracture energy of the ice plate and the whole kinetic energy of the ice plate was negligible as well.
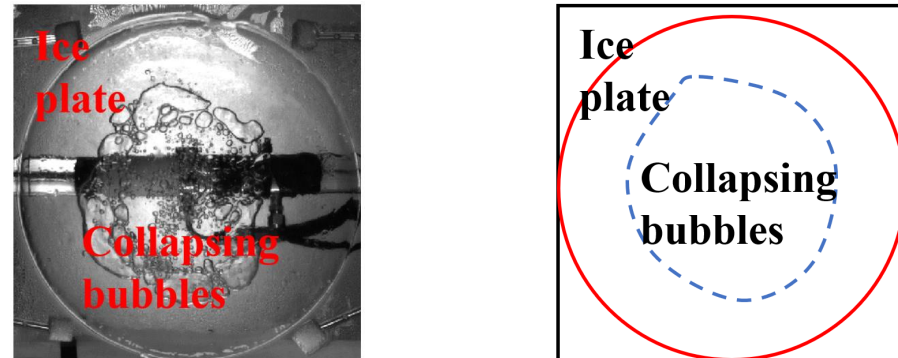

Figure 12. No crack pattern when $H = 1.68$, $T = 0.26$.

3.4. Influence of Parameters

In this study, repeated experiments were carried out to verify repeatability, as shown in Table 1, in which the number was the repeated times in corresponding ranges of H and T. For convenience, distance parameter H was taken as a classification criterion of experimental conditions. When $0 \leq H \leq 0.76$, it was regarded as a small distance condition; when $0.77 \leq H \leq 1.10$, it was considered as a medium distance condition; and when $1.11 \leq H \leq 2.30$, it was regarded as a large distance condition. Due to the difficulties in preparing ice samples, the thicknesses of ice samples from the same batch had slight differences also, but the variation range was very small and within acceptable ranges. At the same time, some defective ice samples could not be used, so the number of experiments varied in Table 1.

Table 1. Different damage patterns of the ice along with distance parameter H and thickness parameter T.

H \\ T	$No.$	0.00–0.17	0.18–0.20	0.21–0.24	0.25–0.26	0.27–0.28	0.29–0.31
Small distance	0.00–0.69	3		5	8	4	1
	0.70–0.76			1	7	4	
Medium distance	0.77–0.84	2		1	7	4	3
	0.85–1.10			4	3 1	0	0
Large distance	1.11–1.40	2		3	2	0	0
	1.41–2.30	3	2	1	0	0	0

Radial and circumferential slits	Radial slits (Shock wave)	Radial slits (Jet)	Radial cracks	No crack

Based on the damage patterns in Section 3.3, Table 1 showed the distribution of current experimental results under different ice thickness parameters T and distance parameters H. Although the results had certain randomness, one could still observe some change rules. Firstly, as one could imagine, when the ice plate was thinner and the distance between the ice and the bubble was smaller, the ice was damaged more seriously. Therefore, most damage patterns were in the upper-left area of the table in brighter colors. Secondly, along with the increase of H, the icebreaking ability of the first shock wave load became

weaker, and the combined effect of secondary shock wave and jet load was significantly enhanced. Thirdly, circumferential cracks were mostly generated at thin ice plates, for example, $T \leq 0.2$ in these experiments. This denoted that a thin ice plate had much smaller allowable radial stress and was easier to be damaged in circumferential cracks based on radial cracks. Last but not least, the 'radial slits' pattern was most common but the 'radial cracks' pattern was quite scarce. This was mainly because the "radial cracks" pattern had very strict conditions for both ice thickness parameters T and distance parameters H simultaneously.

In summary, the underwater airgun bubble can generate multiple loads, including initial and secondary shock waves, bubble jet, and retarded flows, etc. These loads are exerted on the ice plate in sequence and may be superimposed to achieve the best icebreaking effects. Just as mentioned in the introduction, this technology has many advantages such as strong directionality and environmental friendliness, which makes it a potential auxiliary icebreaking method in the fields of polar scientific research, Arctic route development, and ice flood prevention.

3.5. Repeatability and Randomness of the Results

We provided the results of the bubble and its damage effects on ice with same parameters at the same moments, as shown in Figure 13. The parameters in the case were $P_0 = 2.44$ MPa, $h = 70$ mm, $t_{ice} = 20$ mm with dimensionless parameters $H = 0.75$, $T = 0.30$. The case was done twice and adopted to investigate the repeatability and randomness of the results. It can be seen that the evolution of the bubble was almost consistent, which denoted the bubble was relatively stable with parameters. On the other hand, the damage pattern of the ice was also the same, which were both 'radial slits (shock wave)' pattern, although the specific cracks were different. Just as mentioned in a previous study [5], for ice breaking, it was concerned with damage pattern rather than specific crack because of the randomness of crack generation. All these phenomena illustrated the complexity of the ice mechanics [46]. That was also the reason why we were concerned with the damage patterns, but not the specific cracks in Section 3.3.
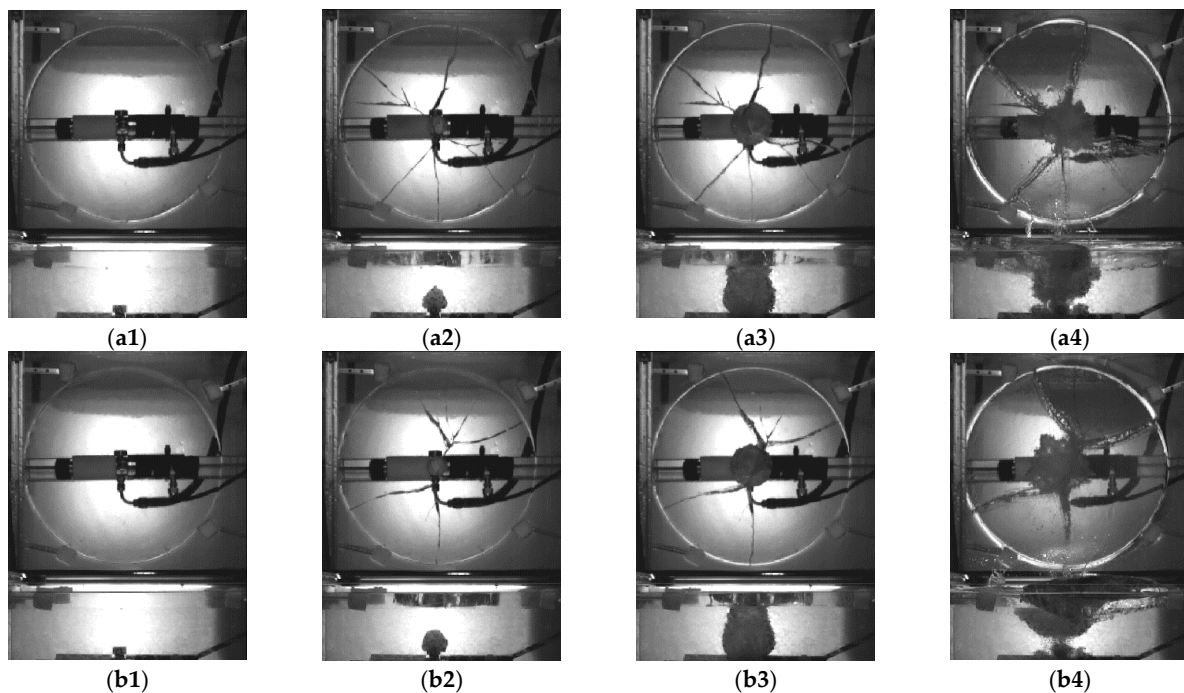
Figure 13. The damage patterns of ice under airgun bubble loads with the same condition $H = 0.75$, $T = 0.30$ ($P_0 = 2.44$ MPa, $h = 70$ mm, $t_{ice} = 20$ mm). (**a1**) $t = 0.00$ ms, (**a2**) $t = 0.90$ ms, (**a3**) $t = 4.50$ ms, (**a4**) $t = 25.00$ ms, (**b1**) $t = 0.00$ ms, (**b2**) $t = 0.90$ ms, (**b3**) $t = 4.50$ ms, (**b4**) $t = 25.00$ ms.

4. Conclusions

Interactions among gas, water, and ice during icebreaking by using an airgun bubble were studied by using a self-designed experimental device. Interfaces among these three media, including bubble surface, free surface, ice wetted surface, captured bubbles, and ice cracks were recorded by the high-speed camera. The main conclusions were drawn as below:

1. Influenced by the airgun structure, the shape of the bubble was not spherical in the expansion stage but presented a unique 'pear-like' shape, which was quite different from the spherical shape of the spark bubble. An initial shock wave was accompanied by the generation of the airgun bubble, followed by oscillatory pressure peaks caused by the directional fast air injection, then cycles of shock waves with damping amplitudes along with the minimum volumes of the bubble. At the same time, a bubble jet and its induced high-pressure peak (even higher than that induced by shock wave) were also observed and measured. The initial shockwave and secondary shockwave together with the jet impact were expected to contribute to the icebreaking mainly.
2. High-pressure airgun bubbles had more cycles underwater than spark bubbles did. As a result, the retarded flow formed by bubble pulsation and collapse played an important role in the process of icebreaking. It aggravated the cracks extending into slits and pushed the ice plate breaking up along the slits. Moreover, once the ice plate separated, a free surface appeared and a spike may have also been generated, which enhanced the effect of icebreaking significantly.
3. There were three typical patterns of icebreaking under the airgun bubble: 'radial slits' pattern, 'radial and circumferential slits' pattern, and 'radial cracks' pattern, under different parameters. For the former two, both initial shock waves and secondary shock wave together with bubble jet can induce these patterns. According to different reasons, the first pattern was further classified as 'radial slits (shock wave)' and 'radial slits (jet)', whereas the second pattern was further classified as 'radial and circumferential (shock wave) slits' and 'radial (shock wave) and circumferential (jet) slits'. The third one was most scarce, as it had very strict conditions for both ice thickness parameters T and distance parameters H simultaneously.
4. The selection of an optimal distance of the bubble is an important problem for practical icebreaking application. It involves many factors, such as ice properties, bubble properties, boundary conditions, etc. As far as the parameters (H and T) concerned in this paper, the smaller the H was, the better the icebreaking effect was. This may be because shockwaves could contribute more at a nearer distance to the ice. Further study on this problem will be continued involving more parameters.

In the future, the effects of more parameters such as surface area and boundary conditions of the ice plate will be considered. Scaling laws to realistic conditions in maritime settings will also be studied, as well as energetic/cost issues.

Author Contributions: Conceptualization, Q.-G.W. and B.-Y.N.; Data curation, Q.-G.W.; Funding acquisition, B.-Y.N. and Y.-Z.X.; Methodology, Q.-G.W., Z.-C.W. and B.-Y.N.; Resources, B.-Y.N. and Y.-Z.X.; Software, G.-Y.Y.; Supervision, B.-Y.N.; Writing—original draft, Q.-G.W. and B.-Y.N.; Writing— review & editing, Y.A.S., Z.-Y.L. and Y.-Z.X. All authors have read and agreed to the published version of the manuscript.

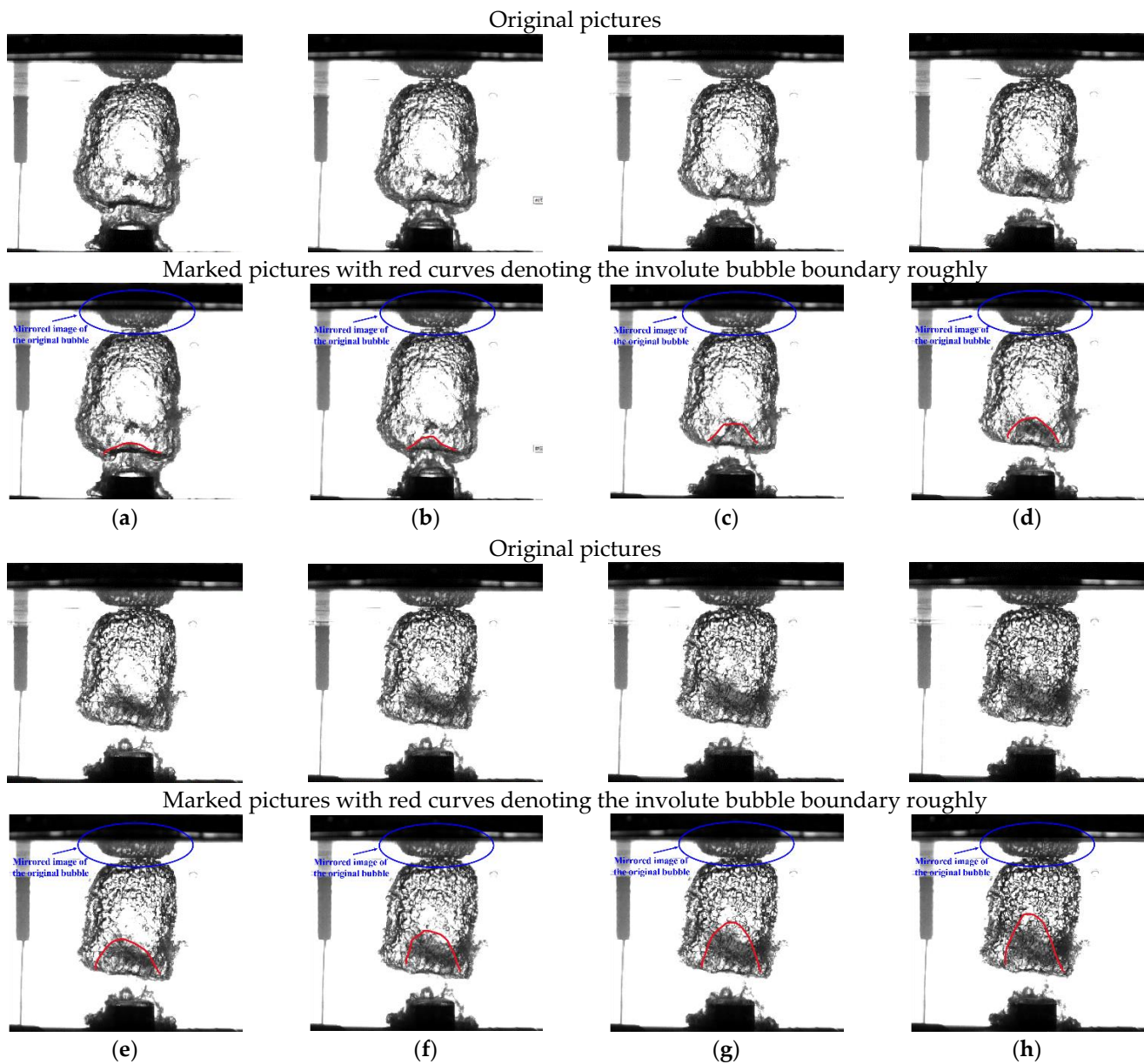**Institutional Review Board Statement:** Not applicable.

Informed Consent Statement: Not applicable.

Data Availability Statement: There are no publicly available data for this study.

Conflicts of Interest: The authors declare no conflict of interest.

Appendix A. The Detailed Development of the Bubble Jet and Volume

Figure A1 shows the development process of the jet of the bubble in Figure 6, in which the involute bubble boundary was also highlighted by red curves in a group of duplicated pictures. As shown in the pictures, one can see that the bubble surfaces were relatively smooth before $t = 8.50$ ms, so the involute bubble surface or the bubble jet was relatively clear and easy to be observed. On the contrast, the bubble surfaces became unsmooth after $t = 8.50$ ms, and the involute bubble surface became blurry and unstable, which was hard to be observed. The red curves can only denote the involute bubble boundary very roughly, which were used to calculated in the bubble volume in Figure A2. As declared in the main text, the bubble structure directly attached to the plate was just a mirrored image of the original bubble, due to the reflection of the smooth aluminum plate surface, which were also marked in Figure A1 by blue circles.

Original pictures

Marked pictures with red curves denoting the involute bubble boundary roughly

(**a**) (**b**) (**c**) (**d**)

Original pictures

Marked pictures with red curves denoting the involute bubble boundary roughly

(**e**) (**f**) (**g**) (**h**)

Figure A1. Images of the jet evolution of the bubble in Figure 6. (**a**) $t = 7.95$ ms, (**b**) $t = 8.15$ ms, (**c**) $t = 8.35$ ms, (**d**) $t = 8.50$ ms, (**e**) $t = 8.65$ ms, (**f**) $t = 8.75$ ms, (**g**) $t = 8.85$ ms, (**h**) $t = 8.95$ ms.

Figure A2 shows the variation of bubble volume in Figure 6. Just as mentioned above in Figure A1, the bubble boundary became very unclear after around t = 8.50 ms, so we just provided the volume change theretofore. One can see the bubble volume rose before fell along with the expansion and contraction of the bubble.
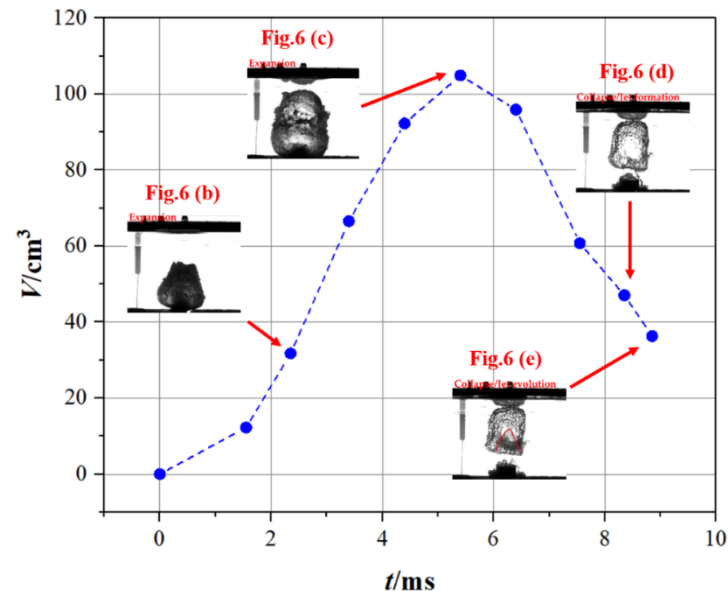

Figure A2. Volume variation of the bubble in Figure 6.

References

1. Sazonov, K.; Dobrodeev, A. Ice Resistance Assessment for a Large Size Vessel Running in a Narrow Ice Channel Behind an Icebreaker. *J. Mar. Sci. Appl.* **2021**, *20*, 446–455. [CrossRef]
2. Ni, B.Y.; Chen, Z.W.; Zhong, K.; Ll, X.A.; Xue, Y.Z. Numerical simulation of a polar ship moving in level ice based on a one-way coupling method. *J. Mar. Sci. Eng.* **2020**, *8*, 692. [CrossRef]
3. Du, Y.; Sun, L.; Pang, F.; Li, H.; Gao, C. Experimental Research of Hull Vibration of a Full-Scale River Icebreaker. *J. Mar. Sci. Appl.* **2020**, *19*, 182–194. [CrossRef]
4. Zhai, M.X.; Li, X.Q.; Hui, F.M.; Cheng, X.; Heil, P.; Zhao, T.C.; Jiang, T.Y.; Cheng, C.; Ci, T.Y.; Liu, Y.; et al. Sea-ice conditions in the Adélie Depression, Antarctica, during besetment of the icebreaker RV Xuelong. *Ann. Glaciol.* **2015**, *56*, 160–166. [CrossRef]
5. Wang, Z.; Turner, J.; Sun, B.; Li, B.; Liu, C. Cyclone-induced rapid creation of extreme Antarctic sea ice conditions. *Sci. Rep.* **2014**, *4*, 5317. [CrossRef]
6. Ni, B.Y.; Wang, Q.; Xue, Y.Z.; Wang, Y.; Wu, Q.G. *Numerical Simulation on the Damage of Ice Floe by High-Pressure Bubble Jet Loads*, 3rd ed.; Workshop and Symposium on Safety and Integrity Management of Operations in Harsh Environments: St. John's, NL, Canada, 2017.
7. Ni, B.Y.; Pan, Y.T.; Yuan, G.Y.; Xue, Y.Z. An experimental study on the interaction between a bubble and an ice floe with a hole. *Cold Reg. Sci. Technol.* **2021**, *187*, 103281. [CrossRef]
8. Cui, P.; Zhang, A.M.; Wang, S.; Khoo, B.C. Ice breaking by a collapsing bubble. *J. Fluid Mech.* **2018**, *841*, 287–309. [CrossRef]
9. Kan, X.Y.; Zhang, A.M.; Yan, J.L.; Wu, W.B.; Liu, Y.L. Numerical investigation of ice breaking by a high-pressure bubble based on a coupled BEM-PD model. *J. Fluids Struct.* **2020**, *96*, 103016. [CrossRef]
10. Yuan, G.Y.; Ni, B.Y.; Wu, Q.G.; Xue, Y.Z.; Zhang, A.M. An experimental study on the dynamics and damage capabilities of a bubble collapsing in the neighborhood of a floating ice cake. *J. Fluids Struct.* **2020**, *92*, 102833. [CrossRef]
11. Jorgensen, J.K.; Gyselman, E.C. Hydroacoustic measurements of the behavioural response of arctic riverine fishes to seismic airguns. *J. Acoust. Soc. Am.* **2009**, *126*, 1598–1606. [CrossRef]
12. Hermannsen, L.; Tougaard, J.; Beedholm, K.; Nabe-Nielsen, J.; Madsen, P.T. Characteristics and propagation of airgun pulses in shallow water with implications for effects on small marine mammals. *PLoS ONE* **2015**, *10*, e0133436. [CrossRef] [PubMed]
13. Chahine, G.L.; Kalumuck, K.M.; Hsiao, C.T. Simulation of surface piercing body coupled response to underwater bubble dynamics utilizing 3DYNAFS, a three-dimensional BEM code. *Comput. Mech.* **2003**, *32*, 319–326. [CrossRef]
14. Goh, B.H.T.; Gong, S.W.; Ohl, S.W.; Khoo, B.C. Spark-generated bubble near an elastic sphere. *Int. J. Multiph. Flow* **2017**, *90*, 156–166. [CrossRef]
15. Chen, H.L.; Ni, B.Y.; Hu, W.J.; Xue, Y.Z. Model experimental study of damage effects of Ship structures under the contact jet loads of bubble in a water tank. *Shock Vib.* **2018**, *2018*, 8456925. [CrossRef]

16. Tatlisuluoglu, A.; Beji, S. Blast Pressure Measurements of an Underwater Detonation in the Sea. *J. Mar. Sci. Appl.* **2021**, *20*, 706–713. [CrossRef]
17. Duan, Y.S.; Wang, X.H.; Liu, S.B. Application of blasting technique to against ice jam. *J. Glaciol. Geocryol.* **2003**, *25*, 220–226.
18. Barash, R.M. *Ice-Breaking by Explosives*; Naval Ordnance Laboratory Technical Report NOLTR 66–29; Naval Ordnance Laboratory: White Oak, MD, USA, 1966.
19. Mellor, M. *Breaking Ice with Explosives*; USA Cold Regions Research and Engineering Laboratory: Hanover, NH, USA, CRREL Report 82-40; 1982.
20. Mellor, M. Derivation of guidelines for blasting floating ice. *Cold Reg. Sci. Technol.* **1987**, *13*, 193–206. [CrossRef]
21. Wang, Y.; Qin, Y.; Yao, X. A combined experimental and numerical investigation on damage characteristics of ice sheet subjected to underwater explosion load. *Appl. Ocean. Res.* **2020**, *103*, 102347. [CrossRef]
22. Wang, Y.; Qin, Y.Z.; Wang, Z.K.; Yao, X.L. Numerical study on ice damage characteristics under single explosive and combination explosives. *Ocean. Eng.* **2021**, *223*, 108688. [CrossRef]
23. Asuelimen, G.; Blanco-Davis, E.; Wang, J.; Yang, Z.L.; Matellini, D.B. Formal Safety Assessment of a Marine Seismic Survey Vessel Operation, Incorporating Risk Matrix and Fault Tree Analysis. *J. Mar. Sci. Appl.* **2020**, *19*, 155–172. [CrossRef]
24. Giles, B.F. Pneumatic acoustic energy source. *Geophys. Prospect.* **1968**, *16*, 21–53. [CrossRef]
25. Chen, Y.; Zhang, X.K.; Qiu, X.L.; Ge, H.K.; Liu, B.J.; Wang, B.S. A new method to generate seismic wave on the land. *Chin. Sci. Bull.* **2007**, *11*, 1317–1321. (In Chinese)
26. Chelminski, S.; Watson, L.M.; Ronen, S. Research Note: Low-frequency pneumatic seismic sources. *Geophys. Prospect.* **2019**, *67*, 1547–1556. [CrossRef]
27. Mellor, M.; Kovacs, A. *Breakage of Floating Ice by Compressed Gas Blasting*; Cold Regions Research and Engineering Laboratory (CRREL): Hanover, New Hampshire, USA, 1972; pp. 1–9, Special Report 184.
28. Coburn, J.L., Jr.; Ehrlich, N.A. Advanced icebreaking concepts. *Nav. Eng. J.* **1973**, *85*, 11–19. [CrossRef]
29. Ni, B.Y.; Wu, Q.G.; Yuan, G.Y. Air Gun Device for Underwater High Pressure Gas Ice-Breaking Experiment. Chinese Patent 109900177, 20 April 2021. (In Chinese).
30. De Graaf, K.L.; Brandner, P.A.; Penesis, I. Bubble dynamics of a seismic airgun. *Exp. Therm. Fluid Sci.* **2014**, *55*, 228–238. [CrossRef]
31. Cheremisinoff, N.P. *Applied Fluid Flow Measurement Fundamentals & Technology*; Marcel Dekker Inc: New York, NY, USA, 1979.
32. Ni, B.Y.; Zhang, A.M.; Wang, Q.X.; Wang, B. Experimental and numerical study on the growth and collapse of a bubble in a narrow tube. *Acta Mech. Sin.* **2012**, *28*, 1248–1261. [CrossRef]
33. Hobbs, P.V. *Ice Physics*; Oxford University Press: Oxford, UK, 1974.
34. Rayleigh, J.W. On the pressure developed in a liquid during the collapse of a spherical cavity. *Philos. Mag.* **1917**, *34*, 94–98. [CrossRef]
35. Willis, H. *Underwater Explosions, Time Interval between Successive Explosions: Report, British Report*; The National Archives: Kew, Richmond, 1941.
36. Wehner, D.; Landr, M.; Amundsen, L. On Low Frequencies emitted by Air Guns at Very Shallow Depths—An Experimental Study. *Geophysics* **2019**, *84*, 61–71. [CrossRef]
37. de Graaf, K.L.; Penesis, I.; Brandner, P.A. Modelling of seismic airgun bubble dynamics and pressure field using the Gilmore equation with additional damping factors. *Ocean Eng.* **2014**, *76*, 32–39. [CrossRef]
38. Yu, Q.; Xu, Z.; Zhao, J.; Zhang, M.; Ma, X. PIV-Based Acoustic Pressure Measurements of a Single Bubble near the Elastic Boundary. *Micromachines* **2020**, *11*, 637. [CrossRef]
39. Carlomagno, G.M.; Ianiro, A. Thermo-fluid-dynamics of submerged jets impinging at short nozzle-to-plate distance: A review. *Exp. Therm. Fluid Sci.* **2014**, *58*, 15–35. [CrossRef]
40. Kitagawa, K.; Nagahiro, D.; Ohtani, K.; Abe, A. *Collision of Underwater Explosion with Compressible Porous Wall*; Springer: Cham, Switzerland, 2019.
41. Cui, X. Experimental Study of Hopkinson Bar Based Measurement Methodology to Wall Pressure Generated by Near-Field Underwater Explosion. Ph.D. Thesis, Harbin Engineering University, Harbin, China, 2019. (In Chinese).
42. Lauterborn, W.; Ohl, C.D. Cavitation bubble dynamics. *Ultrason. Sonochemistry* **1997**, *4*, 65–75. [CrossRef]
43. Lauterborn, W.; Bolle, H. Experimental investigations of cavitation-bubble in the neighbourhood of a solid boundary. *J. Fluid Mech.* **1975**, *72*, 391–399. [CrossRef]
44. Geers, T.L.; Hunter, K.S. An integrated wave-effects model for an underwater explosion bubble. *J. Acoust. Soc. Am.* **2002**, *111*, 1584–1601. [CrossRef]
45. Bazant, Z.P.; Kim JJ, H.; Li, Y.N. Part-through bending cracks in sea ice plates: Mathematical modeling. *Am. Soc. Mech. Eng. Appl. Mech. Div. AMD* **1995**, *207*, 97–105.
46. Bai, X.; Zemlyak, V.; Vasilyev, A.; Kozin, V. Stressed-Deformed State of Ice Crossings at the Surface Reinforcement of Composite Materials. *J. Mar. Sci. Appl.* **2020**, *19*, 430–435. [CrossRef]